

## Article

# Effects of Additional Flexible and Rigid Structure on BDT-BDD Terpolymer and the Performance of Organic Solar Cells

Xin Jing<sup>1,2,3</sup>, Xuebing Li<sup>3</sup>, Yong Zhao<sup>2</sup>, Quanliang Wang<sup>2</sup>, Xiao Kang<sup>2</sup>, Xiaojie Liu<sup>2</sup>, Aziz Saparbaev<sup>4</sup> , Feng Li<sup>1,\*</sup> and Mingliang Sun<sup>2,\*</sup>

<sup>1</sup> Analytical and Testing Center, Qingdao University of Science and Technology, Qingdao 266042, China; jingxin@stu.ouc.edu.cn

<sup>2</sup> School of Materials Science and Engineering, Ocean University of China, Qingdao 266100, China; y.zhao1972@foxmail.com (Y.Z.); wql@stu.ouc.edu.cn (Q.W.); kangxiao1994@126.com (X.K.); liuxiaojie19921005@163.com (X.L.)

<sup>3</sup> Chemistry Department, Paderborn University, 33098 Paderborn, Germany; lixuebing2121@163.com

<sup>4</sup> Institute of Ion-Plasma and Laser Technologies, Uzbekistan Academy of Sciences, 33, Durmon yuli, Tashkent 100125, Uzbekistan; saporbaevaziz83@gmail.com

\* Correspondence: lifeng02@qust.edu.cn (F.L.); mlsun@ouc.edu.cn (M.S.)

**Abstract:** In organic solar cells, the aggregation and crystallization of polymers are significant for bulk heterojunction. Blending with acceptor materials, polymer donor materials can adjust their aggregation by the movement of the chain segments. In this paper, the unfused structures based on thiophene and carbazole are respectively designed and introduced into the donor-acceptor copolymer donor materials to investigate the influence of flexible and rigid structures on polymer-aggregation leading photoelectric performance. The material and quantum chemical property investigations show that the selection and design of the blocks are important for the properties of the terpolymers, and the resulting polymer:Y6 devices achieve improvements in performance from 13.85% to 15.66% (especially for fill factors from 63.37% up to 69.81%). This result contributes to designing and optimizing efficient polymers.

**Keywords:** flexible and rigid structures; terpolymers; conformation adjustment; organic solar cells



Academic Editor: Muhammad Salahuddin Khan

Received: 18 December 2024

Revised: 15 January 2025

Accepted: 16 January 2025

Published: 20 January 2025

**Citation:** Jing, X.; Li, X.; Zhao, Y.; Wang, Q.; Kang, X.; Liu, X.; Saparbaev, A.; Li, F.; Sun, M. Effects of Additional Flexible and Rigid Structure on BDT-BDD Terpolymer and the Performance of Organic Solar Cells. *Polymers* **2025**, *17*, 248. <https://doi.org/10.3390/polym17020248>

**Copyright:** © 2025 by the authors. Licensee MDPI, Basel, Switzerland. This article is an open access article distributed under the terms and conditions of the Creative Commons Attribution (CC BY) license (<https://creativecommons.org/licenses/by/4.0/>).

## 1. Introduction

For bulk heterojunction (BHJ) organic solar cells (OSCs), the organization and morphology of the active layer are intimately related to the photoelectric performance [1–3]. Current popular non-fullerene small-molecule acceptor materials, whether ITIC or Y6-series, often need to be finely optimized for forming a reasonable active material stacking or crystallization, significantly improving device performance [4]. For example, thermal annealing of the active layers can promote the phase segregation of the donor and acceptor materials to achieve the optimal morphology of the BHJ, while solvent evaporation treatment is to better self-organize the materials in nanodomains [5]. However, controlling requires careful attention. On the one hand, insufficient or poor aggregation behavior will suppress exciton separation by poor phase separation [6]. On the other hand, excessive phase separation also leads to excessive crystalline regions, resulting in reduced donor-acceptor material interfaces and poor OSC performance [7]. Therefore, reasonably optimizing the active layer to function in the best state is significant in OSC research.

The general approach to BHJ optimization includes three channels. Firstly, pre-treatment of the BHJ-forming solution, including volatile additive incorporation, ternary

blending, heat or cold treatment of the film-forming solution, etc. Secondly, post-treatment of the BHJ active layer, such as thermal annealing, solvent evaporation treatment, etc., and thirdly, optimizing molecule structures, i.e., modifying active materials molecule structures to retain the light absorption properties and improve the aggregation and crystallization properties. BHJ film forms in a non-equilibrium morphology within several seconds, molecule conformations and leading self-organized aggregation are frozen. Thus, morphology modification depends on polymer-chain mobility [8]. No matter the methods, the aim is to adjust the molecular conformation by changing the conditions, which regulates aggregation by balancing molecular interactions. However, adjusting the molecular conformation and regulating molecular aggregation need enough energy to turn an appropriate aggregation morphology, which is decided by chemical structures. Thus, optimizing molecule structures is important.

Optimizing molecule structures can fundamentally solve the problem of active layer morphology, which avoids the tedious processes involved in pre-treatment or post-treatment in the industry. In addition to branched-chain engineering of molecules, modifying the molecular backbone can also have unexpected effects. For example, by linkage engineering, the conformations of terminal-linked dimers can invert from rigid to flexible, which has a distinct influence on photovoltaic performance [9]. For donor polymers, the backbones are controlled by the structural units. For example, thiophene and benzene are the two most fundamental blocks along polymer chains; however, thiophene-thiophene linkages tend to exhibit higher planarity than benzene-benzene linkages [10]. Furthermore, polymer crystallization can be adjusted by randomly distributing irregular structural units along the sequence of the chain [11]. The intrinsic structural properties of polymer chains, such as different degrees of conformational and configurational freedom and chain stiffness, determine how crystalline or amorphous the polymeric materials are intrinsically and how important kinetic factors are in impacting ordering in specific fabrication procedures [12]. From this point, random terpolymers can combine the local conformation regulating and the excellent binary polymer properties into the polymer backbone by optimizing structural units [13]. Flexible or rigid, structural units will improve polymer conformations, which influences the self-assembled block and the lead crystalline of polymers.

In this paper, with ester-substituted thiophene as  $\pi$ -bridges, the unfused units (3T and 2TKZ) based on thiophene and carbazole were designed, respectively. Composed of benzo[1,2-b:4,5-b']dithiophene (BDT) and benzo-[1,2-c:4,5-c]dithiophene-4,8-dione (BDD) blocks, polymers with BDT-BDD backbones exhibit strong aggregation behavior [14]. Oligothiophenes are the most frequently used material due to their flexibility and high charge-carrier mobility. The mobility of thiophene-based copolymers can be improved by incorporating a rigid fused unit, which provides a polymer with higher crystallinity and a more ordered morphology [15,16]. Thus, the 3T and 2TKZ are introduced into BDT-BDD chains and the influence of flexible and rigid structures on polymer-aggregation of synthesized terpolymers is investigated. It finds that the type and content of introduced structures can regulate polymer aggregation. As a result, the photovoltaic performance of terpolymers is improved. In 3T-terpolymer-based OSC devices, the power conversion efficiency (PCE) can improve from 13.85% to 15.66%, especially in fill factor (FF, from 63.37% to 69.81%). It demonstrates the significance of optimizing flexible and rigid molecule structures for bulk heterojunction (BHJ).

## 2. Materials and Methods

### 2.1. Materials and Synthesis

Monomers such as (4,8-bis(4-chloro-5-(2-ethylhexyl)thiophen-2-yl)benzo[1,2-b:4,5-b']dithiophene-2,6-diyl)bis(trimethylstannane) (BDT-Sn(Me)<sub>3</sub>), 1,3-bis(5-bromothiophen-

2-yl)-5,7-bis(2-ethylhexyl)-4H,8H-benzo[1,2-c:4,5-c']dithiophene-4,8-dione (BDD-Br), and 2-bromothiophene-3-carboxylic acid are purchased (Derthon Optoelectronic Materials Science Technology Co., Ltd., Shenzhen, China) and used without further purification.

#### **Decyl 2-bromothiophene-3-carboxylate (A)**

2-bromothiophene-3-carboxylic acid (2.07 g, 10 mmol), dicyclohexylcarbodiimide (2.27 g, 11 mmol), and 4-dimethylaminopyridine (0.5 g, 4.1 mmol) were dissolved in DCM (10 mL), followed by the addition of n-decanol (2.37 g, 15 mmol) and stirring at room temperature for 50 h. After reaching the reaction time, the organic phase was collected by adding water (100 mL) and extracting it with DCM. The organic phase was dried over anhydrous Na<sub>2</sub>SO<sub>4</sub> and the solvent was removed using a rotary evaporator to obtain crude compound A. Crude compound A was purified by silica gel column chromatography using PE/DCM as eluent (PE/DCM = 6/1, *v/v*). The final colorless and clear liquid A was obtained. (2.74 g, yield 79%).

<sup>1</sup>H NMR (600 MHz, CDCl<sub>3</sub>) δ 7.37 (d, 1H), 7.21 (d, 1H), 4.28 (t, 2H), 1.74 (m, 2H), 1.43 (m, 2H), 1.26 (m, 12H), 0.88 (t, 3H).

#### **Didecyl [2,2':5',2''-terthiophene]-3,3''-dicarboxylate (B)**

Compound A (1.04 g, 3 mmol), 2,5-bis(trimethylstannyl)thiophene (0.61 g, 1.5 mmol), and Pd(PPh<sub>3</sub>)<sub>4</sub> (0.17 g, 0.15 mmol) were dissolved in dry toluene (15 mL) under N<sub>2</sub> protection and stirred at reflux for 48 h. After reaching the reaction time, the heating was stopped and the reaction was cooled down naturally to room temperature. After reaching the reaction time, the heating was stopped and cooled down naturally to room temperature. The solvent was removed from the mixture using a rotary evaporator. The crude compound B was purified by silica gel column chromatography using PE/DCM (PE/DCM = 4/1, *v/v*) as eluent. The obtained colorless and clear liquid B. (0.81 g, yield 87%).

<sup>1</sup>H NMR (600 MHz, CDCl<sub>3</sub>): 7.50 (d, 2H), 7.39 (s, 2H), 7.21 (d, 2H), 4.24 (t, 4H), 1.68 (m, 4H), 1.24 (m, 28H), 0.87 (t, 6H).

#### **Didecyl 5,5''-dibromo-[2,2':5',2''-terthiophene]-3,3''-dicarboxylate (C)**

Compound B (0.62 g, 1 mmol) was dissolved in CHCl<sub>3</sub> (20 mL) under N<sub>2</sub> protection and protected from light, followed by the addition of NBS (0.45 g, 2.5 mmol) to the solution. The reaction was carried out under stirring conditions at room temperature and protected from light for 48 h. After reaching the reaction time, the organic phase was collected by adding water (100 mL) and extracted with DCM. The collected organic phase was dried with anhydrous Na<sub>2</sub>SO<sub>4</sub>. Finally, the solvent was removed using a rotary evaporator to obtain crude compound C. Crude compound C was purified by silica gel column chromatography using PE/DCM (PE/DCM = 3/1, *v/v*) as eluent. A yellow solid C was finally obtained. (0.71 g, yield 92%).

<sup>1</sup>H NMR (600 MHz, CDCl<sub>3</sub>): 7.44 (s, 2H), 7.34 (s, 2H), 4.22 (t, 4H), 1.67 (m, 4H), 1.25 (m, 28H), 0.88 (t, 6H).

#### **Didecyl 2,2'-(9-(2-ethylhexyl)-9H-carbazole-2,7-diyl)bis(thiophene-3-carboxylate) (D)**

Compound D was synthesized in the same way as B. Only 2,5-bis(trimethylstannyl)thiophene was replaced by 9-(2-ethylhexyl)-2,7-bis(trimethylstannyl)-9H-carbazole and the same molar was used for each reactant in the synthesis. (0.96 g, yield 79%)

<sup>1</sup>H NMR (600 MHz, CDCl<sub>3</sub>): 8.08 (d, 2H), 7.56 (d, 2H), 7.52 (s, 2H), 7.37 (d, 2H), 7.28 (d, 2H), 4.18 (m, 2H), 4.12 (t, 4H), 2.10 (m, 1H), 1.48 (m, 4H), 1.25 (m, 36H), 0.86 (m, 12H).

#### **2,8-Dibromo-10,11-bis(2-ethylhexyl)-10,11-dihydro-[1,2,5]thiadiazolo[3,4-e]thieno[2',3':4,5]pyrrolo[3,2-g]thieno[3,2-b]indole (E)**

Compound E is synthesized in the same way as C. Only B was replaced by D and the same molar was used for each reactant in the synthesis. (0.81 g, yield 83%)

$^1\text{H}$  NMR (600 MHz,  $\text{CDCl}_3$ ): 8.29 (s, 2H), 7.61 (d, 2H), 7.40 (s, 2H), 7.36 (d, 2H), 4.10 (d, 2H), 4.04 (t, 4H), 2.00 (m, 1H), 1.57 (m, 4H), 1.24 (m, 36H), 0.86 (m, 12H).

### SFZn-x

Terpolymers SFZn-x were fabricated using an identical process except for the acceptor monomer. SFZ1-0.2 was synthesized by BDT-Sn(Me)<sub>3</sub> (0.1 mmol, 97.3 mg), BDD-Br (0.08 mmol, 61.3 mg), and monomer C (0.02 mmol, 15.5 mg). SFZ1-0.4 was synthesized by BDT-Sn(Me)<sub>3</sub> (0.1 mmol, 97.3 mg), BDD-Br (0.06 mmol, 46.0 mg), and monomer C (0.04 mmol, 30.1 mg). SFZ2-0.2 was synthesized by BDT-Sn(Me)<sub>3</sub> (0.1 mmol, 97.3 mg), BDD-Br (0.08 mmol, 61.3 mg), and monomer E (0.02 mmol, 19.4 mg). Monomers were dissolved in toluene (10 mL). Pd(PPh<sub>3</sub>)<sub>4</sub> (20 mg) was added to the mixtures. The reactions were stirred at 110 °C for 48 h under N<sub>2</sub>. The polymers were precipitated in methanol (100 mL) and filtrated. The precipitates were purified by a Soxhlet extractor with PE, DCM, and CF as eluent. The polymer was then precipitated in methanol (60 mL) and dried under a vacuum for 24 h before use.

### PBDB-T-2Cl

PBDB-T-2Cl is synthesized in the same way as SFZn-x. the only difference is BDD-Br and BDT-Sn(Me)<sub>3</sub> are used in same molar equivalent.

## 2.2. Characterization of Physical Property

The electrochemical linear sweep voltammetry (LSV) was recorded with a computer-controlled electrochemical workstation (Chen Hua CHI600e, Shanghai, China) using a polymer drop-cast film on glassy carbon electrode as the working electrode, platinum wire as the counter electrode and saturated calomel electrode as the reference electrode. 0.1 M Bu<sub>4</sub>NPF<sub>6</sub> dissolved in acetonitrile was used as the supporting electrolyte. Oxidation processes were measured from 0 V to 1.5 V and reduction processes from 0 V to -1.5 V, scan rate sets to 0.05 V s<sup>-1</sup>. The results were corrected by Fc/Fc<sup>+</sup>.

OSCs were fabricated in the conventional structure of ITO/PEDOT:PSS/polymer:Y6/PDINO/Al. The substrates were cleaned using detergent, deionized water, acetone, and isopropanol every 15 min, and then treated in ultraviolet ozone for 3 min. This is followed by spin coating a thin layer of PEDOT:PSS on the precleaned ITO-coated glass substrates at 4000 rpm for 30 s and then annealed at 150 °C for 15 min. Then, the substrates were transferred into a glovebox. Afterward, for the BHJ devices, the optimized active layer was spin-coated from CHCl<sub>3</sub> solution with a sum concentration of 15.7 mg mL<sup>-1</sup> (D:A =1:1.2) at 3200 rpm for 30 s to form an active layer. The fabricated active layer was spin-coated by 1 mg mL<sup>-1</sup> PDINO solution (methanol as solvent) at 3000 rpm for 30 s. After physical vapor depositing an 80-nm-thick Al electrode on the PDINO interface layer, OSCs were fabricated.

The current density-voltage (J-V) characteristics were measured in the glovebox under AM 1.5 G spectra (100 mW cm<sup>-2</sup>) from a solar simulator (Keithley 2400, Beaverton, OR, USA). The light intensity was calibrated with a 20 mm × 20 mm monocrystalline silicon reference cell. The J-V curves are measured along the forward scan direction from -1.5 to 1.5 V. A solar cell spectral response measurement system (QE-R3011, Kaohsiung, Taiwan) measured the EQE. The light intensity at each wavelength was calibrated with a standard single-crystal Si photovoltaic cell.

## 3. Results and Discussion

Two unfused structures (3T and 2TKZ) are designed and synthesized based on thiophene and 9-(2-ethylhexyl)-9H-carbazole, which linked two decyl thiophene-3-carboxylate (T), respectively [17,18]. Terpolymers SFZn-x (Figure 1) are obtained by randomly and partly replacing BDD units with 3T or 2TKZ in the strong-aggregation BDT-BDD backbones. The n in SFZn-x corresponds to the type of second acceptor units, and x is for the con-

tent. For example, SFZ1-0.4 is synthesized by 1 equivalent BDT, 0.6 equivalent BDD, and 0.4 equivalent 3T monomers, while SFZ2-0.2 is obtained by the ratio of 1, 0.8, and 0.2 in BDT, BDD, 2TKZ. The synthesis of the monomers is shown in the Supplementary Information.

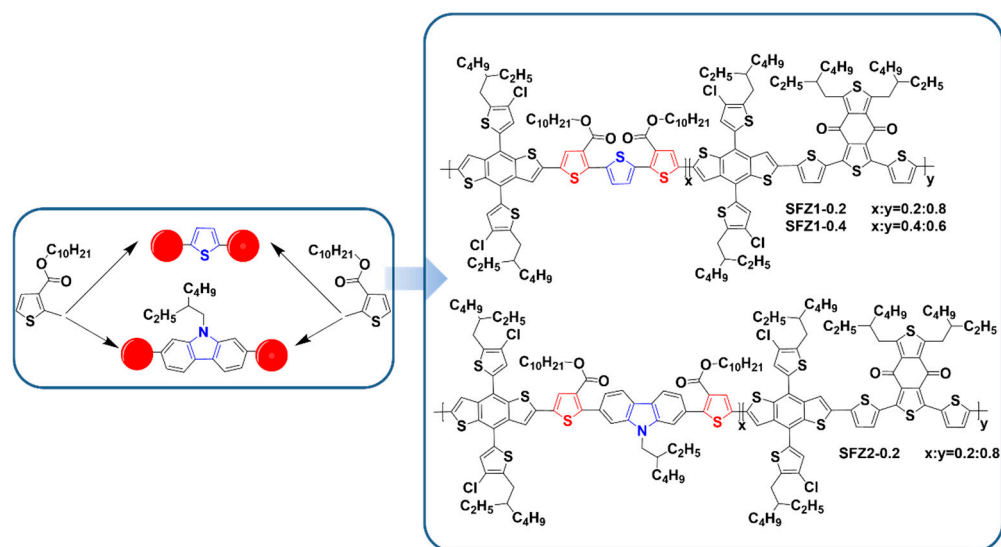


**Figure 1.** The molecular formula of SFZn-x terpolymers.

The electrochemical linear sweep voltammetry (LSV) curves of SFZn-x for their onset oxidation and reduction potential ( $E_{\text{onset(OX.)}}$  and  $E_{\text{onset(RED.)}}$ ) are shown in Figure S1. The estimated highest occupied molecular orbital (HOMO) and lowest unoccupied molecular orbital (LUMO) energy levels by  $E_{\text{onset(OX.)}}$  and  $E_{\text{onset(RED.)}}$  are presented in Figure 2a and Table 1. Terpolymers and their parent polymer PBDB-T-2Cl reveal similar HOMO energy levels, while LUMO energy levels are slightly upward-shifted for the SFZ2-0.2 than others. This may be related to differences in chemical structure.

**Table 1.** Optical and electrochemical properties of SFZn-x terpolymers.

Polymer	HOMO (eV) <sup>a</sup>	LUMO (eV) <sup>a</sup>	$\lambda_{\text{onset}}$ (nm) <sup>b</sup>	$\lambda_{\text{onset}}$ (nm) <sup>c</sup>	$E_g$ (eV) <sup>c</sup>	$\Delta\lambda_{0-1}$ (nm) <sup>d</sup>
SFZ1-0.2	−5.55	−3.43	659	672	1.85	24
SFZ1-0.4	−5.60	−3.41	651	677	1.83	30
SFZ2-0.2	−5.53	−3.26	662	676	1.83	22

<sup>a</sup> Measured from LSV, where  $E_{\text{HOMO/LUMO}}$  (eV) =  $-(E_{\text{onset(OX./RED.)}} - E_{\text{Fc}^+/\text{Fc}} + 4.8)$ ,  $E_{\text{Fc}^+/\text{Fc}} = 0.36$  V. <sup>b</sup> Measured from solution state. <sup>c</sup> Measured from film state and estimated by  $E_g$  (eV) =  $1240/\lambda_{\text{onset}}$ . <sup>d</sup>  $\Delta\lambda_{0-1}$  (nm) =  $\lambda_{0-1}$  (20 °C) −  $\lambda_{0-1}$  (100 °C).

The Ultraviolet-visible (UV-vis) absorption spectra of SFZn-x in solution and film are shown in Figure 2b,c. Absorptions possess similar profiles in solution and film, respectively. Film absorptions ( $\lambda_{\text{onset}}$ , the onset wavelength, at 670~680 nm) are red-shifted compared to solution absorptions ( $\lambda_{\text{onset}}$  at 650~665 nm). Similar film absorptions ( $\lambda_{\text{onset}}$ ) imply approaching energy gaps ( $E_g$ ) of around 1.84 eV (Table 1). Their strong saddle-shaped absorption at 450~700 nm can be divided into two absorption peaks: the 0-0 ( $\lambda_{0-0}$ , wavelength of 0-0 peaks, at ~610 nm) are associated with molecular stacking and the 0-1 ( $\lambda_{0-1}$ , wavelength of 0-1 peaks, at ~560 nm) are originated from intramolecular charge transfer. After normalizing according to the intensity of the 0-1 peaks, all absorption spectra expose differences in 0-0 peaks. As the solution (Figure 2b), the 0-0 peak of SFZ1-0.2 is higher than that of SFZ1-0.4, while the 0-0 peak of SFZ2-0.2 is higher than that of SFZ1-0.2. Film absorptions possess consistent trends. The 0-0 peak allows a qualitative comparison of the polymer pre-aggregation, which implies the regulations of molecular aggregation by

the type and content of introducing structures in BDT-BDD backbones. In addition, the blue-shifted absorptions of the SFZ1-0.4 in Figure 2b,c imply its weak aggregation [19].

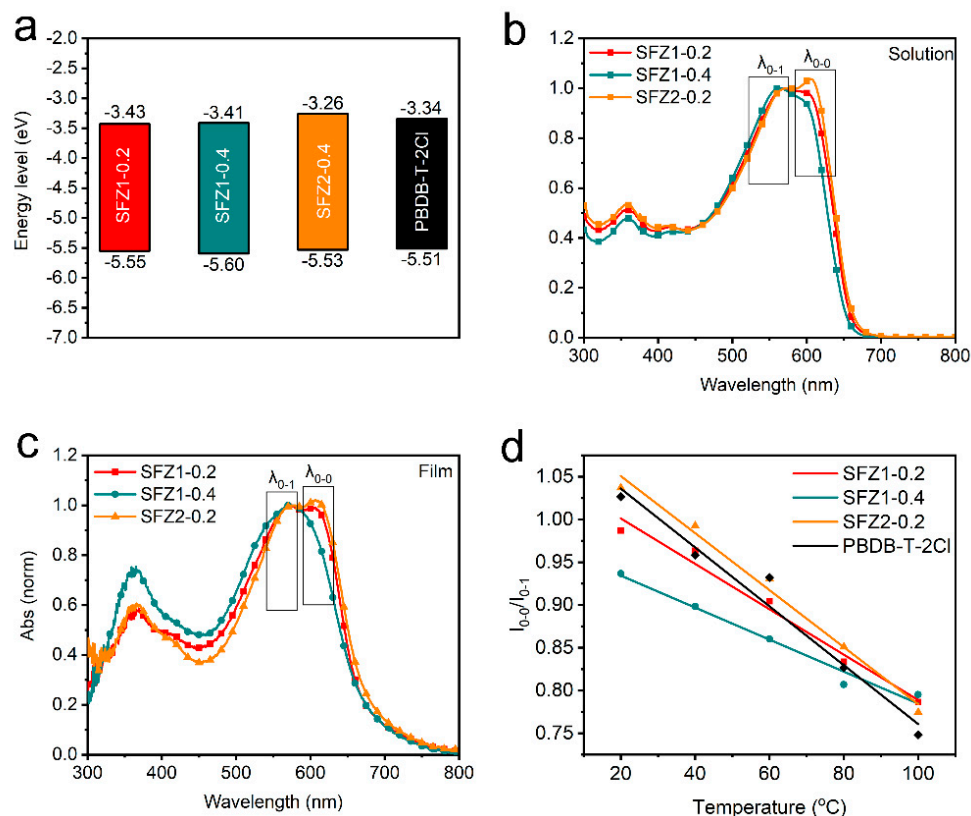


**Figure 2.** (a) Energy levels from LSV curves, absorption in (b) solution and (c) film, and (d) dependence of temperature- $I_{0-0}/I_{0-1}$  from UV-vis absorption at different temperatures.

The normalized UV-vis absorption spectra explore aggregation–temperature relationships of terpolymers at 20, 40, 60, 80, and 100 °C (Figure S2). As the temperature increases, the absorption of SFZn-x and PBDB-T-2Cl blue-shifts, while the 0-0 peak decreases. Therefore, the aggregation of terpolymers formed in a low-temperature solution tends to de-aggregate at high temperatures. The blue-shifted 0-1 peak with increasing temperature corresponds to the adjusted planarization of the polymer backbone [20]. Here, the ratio  $I_{0-0}/I_{0-1}$  of the 0-0 to 0-1 peak intensity and the difference  $\Delta\lambda_{0-1}$  of  $\lambda_{0-1}$  between 20 and 100 °C is defined to quantify the de-aggregation and adjusted planarization. SFZ1-0.4 indicates the highest polymer backbone adjustability with the highest  $\Delta\lambda_{0-1}$  in Table 1. Therefore, the 3T structure is favorable for increasing the flexibility of the polymer backbone. As shown in Figure 2d, the  $I_{0-0}/I_{0-1}$  of the terpolymers decreases quasi-linearly with increasing temperature. At 20 °C, the  $I_{0-0}/I_{0-1}$  values differed significantly. SFZ2-0.2 indicates the highest  $I_{0-0}/I_{0-1}$  ratio, exceeding 1, while SFZ1-0.4's is the lowest. As the temperature increases, the  $I_{0-0}/I_{0-1}$  ratios of three terpolymers tend to close. At 100 °C, their  $I_{0-0}/I_{0-1}$  values are almost equal. The aggregation of the SFZn-x terpolymers is regulated by temperature. At low temperatures, the introduced structure dominates the aggregation behavior of the polymers, which leads to different behaviors. In contrast, the polymers obtain enough energy at high temperatures to de-aggregate, and the dominant BDT-BDD structure becomes the main factor affecting the aggregation behavior. Notably, the  $I_{0-0}/I_{0-1}$  of PBDB-T-2Cl is lower than that of SFZ2-0.2 and higher than that of SFZ1-0.2 and SFZ1-0.4, suggesting enhanced aggregation of 2TKZ and weakened aggregation of 3T in the polymer backbone.

Chain structures play a primary role in determining the physical behaviors of polymers, which often serve as the thermodynamic driving force for structural phase transitions. Thus, the conformations of SFZn-x are simplified as BDT-(3T or 2TKZ)-BDT-BDD with two D-A units, which is to speculate on the modulation of polymer stacking behavior by 3T or 2TKZ under the  $r^2$ SCAN-3c/def2-mTZVPP level using the ORCA 5.0.1 program [21–27]. Also, a simplified BDT-BDD-BDT-BDD structure, labeled RAW, is explored, which represents the PBDB-T-2Cl chain. And SFZ1 and SFZ2 are reminded as the chains of BDT-3T-BDT-BDD, BDT-2TKZ-BDT-BDD, respectively (Figure S3a). The optimized conformations are shown in Figure 3a. The dihedral angle between the two adjacent conjugated building blocks is one of the most critical issues affecting polymer aggregation [28]. The dihedral angles between the units located in the middle of the conformation are summarized in Table S1 (D). In SFZ1 and SFZ2, their backbones form distorted conformations, and the dihedral angles associated with the ester-substituted thiophene are much higher ( $\angle 1 > 20^\circ$  and  $\angle 2 > 30^\circ$ ) than RAW ( $\angle 1, \angle 2 \approx 10^\circ$ ). High  $\angle 1$  and  $\angle 2$  in SFZ1 and SFZ2 are due to the single-bond internal rotation and hindered rotation crossing ester-substituted thiophene.  $\angle 1$  in SFZ1 and SFZ2 are almost equal, while  $\angle 2$  in SFZ1 is slightly larger than that in SFZ2, which may be related to the extended space decreasing hindered interaction between two esters. The above results imply that the size of the thiophene or carbazole core unit introduced affects chain conformation. The energy levels and orbital distributions of HOMO and LUMO are shown in Figure 3b. SFZ1 and SFZ2 have approached HOMO and LUMO energy levels, where both SFZ2's are slightly upshifted compared to that of SFZ1. This result is consistent with the trend estimated by the LSV method. It is worth noting that LUMO and HOMO are distributed primarily in the BDD and BDT units, respectively. The proportion of orbital distributions near the 3T and 2KZ units is small, which suggests that the introduced units do not have much effect on the HOMO and LUMO.

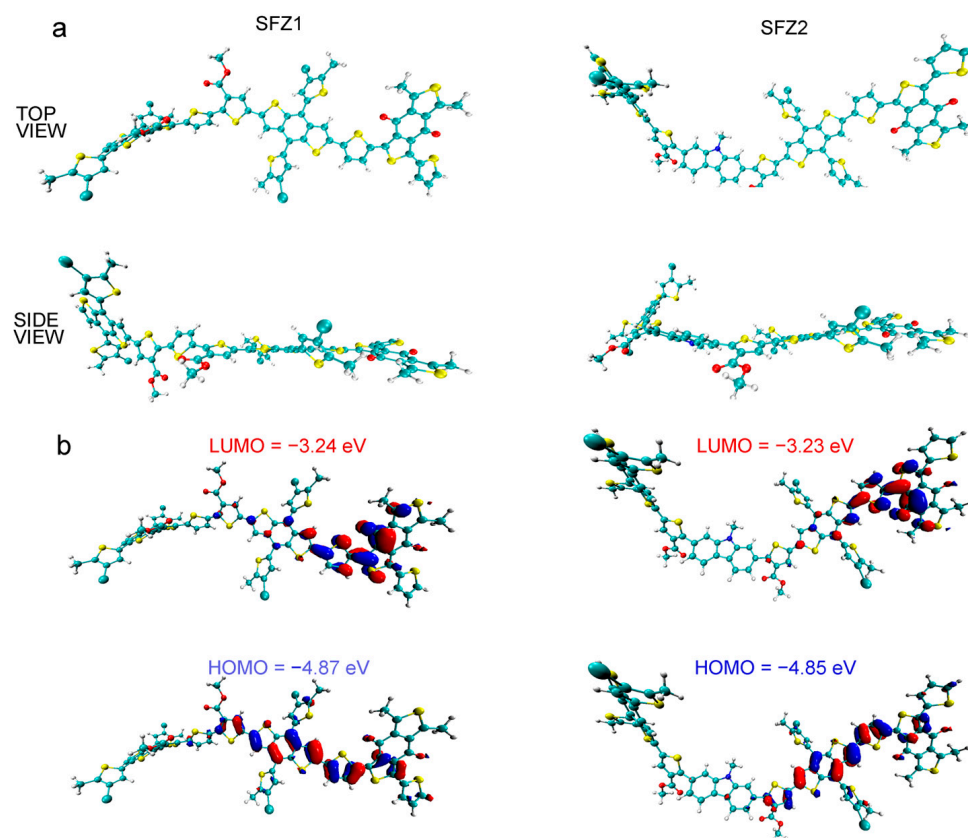
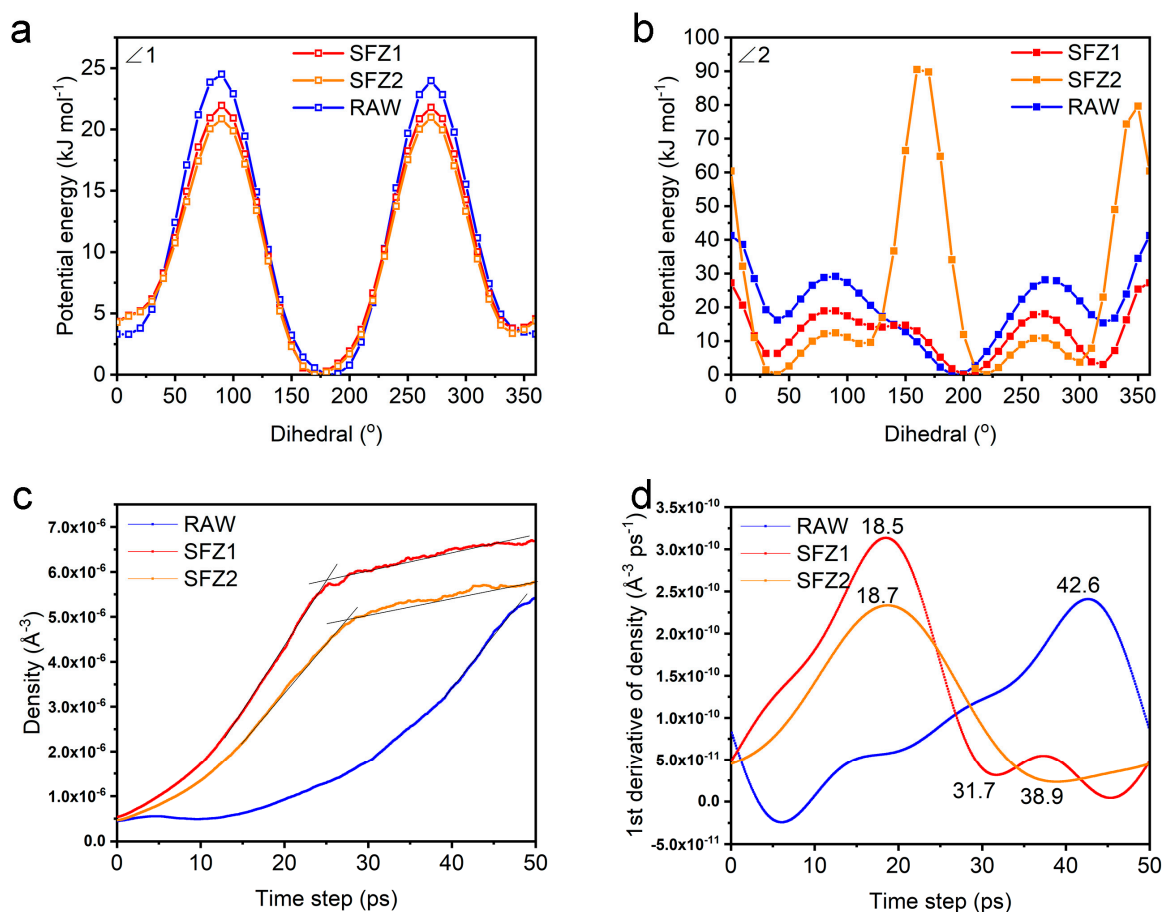


Figure 3. (a) The optimized conformations and (b) HOMO and LUMO of SFZ1 and SFZ2.

A polymer chain possesses semi-flexibility, which characterizes the intra-chain interactions for the most stable conformation persisting along the chain axis. The most common factor that may determine polymer semi-flexibility is internal rotation. The relative potential energy curves of the internal dihedral angles  $\angle 1$  and  $\angle 2$  are obtained by rigid scanning (Figure S4). The  $\angle 1$  curves are saddle-shaped around  $0^\circ \sim 360^\circ$ . The peaks and the troughs are located at  $\sim 90^\circ/270^\circ$  and  $\sim 0^\circ/180^\circ$ , respectively. The  $\angle 2$  curves are complex with  $\sim 90^\circ/270^\circ$  peaks and  $\sim 30^\circ/200^\circ/310^\circ$  troughs. The thermodynamic equilibrium based on the relative energy potential ( $\Delta\epsilon$ ) at troughs defines the static flexibility, and the transition kinetics based on the activation energy ( $\Delta E$ ) at peaks defines the dynamic flexibility of polymer chains. The  $\Delta\epsilon$  and  $\Delta E$  are summarized in Table S2. For  $\angle 1$ , SFZ1, SFZ2, and RAW possess similar  $\Delta\epsilon$ , but  $\Delta E$  of SFZ1 and SFZ2 are lower; for  $\angle 2$ , SFZ1 and SFZ2 show slightly higher  $\Delta\epsilon$  but significantly lower  $\Delta E$ . Polymer chains will exhibit random coils with high flexibility at low  $\Delta\epsilon$  but high rigidity at high  $\Delta\epsilon$ . They can easily change their conformation leading to a fluid state. If changing conformations are hindered, polymers are either in the glass or crystalline in the solid state [11]. Therefore, according to Table S2, SFZ2 is the most flexible and least crystallizable, while RAW is the most rigid and crystallizable. However, in Figure 4a,b, the curve of  $\angle 1$  is more symmetric at  $180^\circ$  than that of  $\angle 2$ .  $\angle 2$  shows another peak at  $\sim 150^\circ$ , which is in descending order of intensity, SFZ2, SFZ1, and RAW. A rigid main chain may limit the conformational behavior of polymers [29]. The high rotational potential energy of SFZ2 results in its conformation fixing in a limited range, exhibiting the highest rigidity and crystallinity, while SFZ1 exhibits the most flexibility and is less crystallizable. Accordingly, the 3T fragment in the polymer increases the flexibility and leads to less crystallizable, while 2TKZ enhances the rigidity and crystallinity. This result is consistent with the fact that SFZ1-0.4 indicates less aggregation but SFZ2-0.2 is more aggregation as demonstrated in UV.

The conformations of polymers were evaluated with molecular dynamics (MD) simulations by the Large-Scale Atomic/Molecular Massively Parallel Simulator (LAMMPS) program [30,31] for the model oligomers 4-D-A-unit (D-A-D-A-D-A-D-A) as RAW, SFZ1, and SFZ2 (Figure S3c). The simulation box contained 30 oligomers distributed randomly in  $150 \times 150 \times 150 \text{ \AA}^3$ . The atom file was generated with Auxiliary Tools of Force Field (AuToFF) [32] and the Packing Optimization for Molecular Dynamics Simulations (Packmol) program [33] by All-atom force fields OPLS-AA/L [34,35]. Each model oligomer was simulated at 300 K and 0 atm in the NPT. Figure 4c shows the density curves of the simulation during equilibration at 50 ps. All densities of the model oligomers continued to grow. After rapid growth, the densities of SFZ1 and SFZ2 slowly increased with fluctuations, indicating that the system tends to equilibrate; however, at the end of the simulation, RAW still did not exhibit a clear equilibrium trend. Figure 4c corresponds to the rate of density change. In 50 ps, all oligomers experienced a maximum, with SFZ1 being the first to reach it, followed by SFZ2, and the RAW reached its maximum only at the end. In addition, SFZ1 began to enter relative equilibrium at  $\sim 32$  ps, SFZ2 was not in relative equilibrium until  $\sim 39$  ps, and RAW did not exhibit a similar state until the end. The equilibrium of the density profile corresponded to the equilibrium system. The system reached equilibrium from nonequilibrium in the shortest time for SFZ1, indicating that its conformational adjustment was the easiest. This result is in agreement with the previous one. In addition, it also implies that both flexible (3T) and rigid (2TKZ) structures can facilitate the conformational adjustment of polymers.



**Figure 4.** The intramolecular dihedral angles of polymers ( $\angle 1$  for the dihedral angle between the BDT donor unit and  $\pi$ -bridge,  $\angle 2$  for the dihedral angle between the acceptor unit and  $\pi$ -bridge), and the potential energy curve of the internal rotation (a)  $\angle 1$  and (b)  $\angle 2$  of polymers. (c) Density-time plots of polymer equilibrium processes and corresponding (d) derivative curves obtained by molecular dynamics.

Based on the above results, the role of the additional unit is mainly to readjust the backbone conformation by internal rotation. For the effect of this internal rotation on the morphology of the blending film, the conformation of the terpolymer with Y6 was explored, which is the most important component of the blending film. The structures of the terpolymers were simplified to BDT-(3T or 2TKZ), and the conformation of donor:accepter (D:A) was explored by the BDT-(3T or 2TKZ):Y6. As a control, BDT-BDD:Y6 was applied as RAW:Y6. The optimized D:A conformations are shown in Figure S5. SFZ1 and SFZ2 exhibited high planarity leading to a face-to-face stacking conformation with Y6. The dihedral angles of the BDT-(3T or 2TKZ) structure in D:A are listed in Table S1 (D:A). Compared to Table S1 (D), both  $\angle 1$  and  $\angle 2$  of SFZ1 and SFZ2 in the D:A were reduced, showing the tuning of polymer conformation due to intermolecular interactions. Notably,  $\angle 1$  and  $\angle 2$  of SFZ1 decreased more drastically, suggesting that the SFZ1 is more prone to conformational adjustment by internal rotation. Thus, the 3T fragment is flexible and 2TKZ enhances the rigidity. This is consistent with the rigidity scan results. Among D:A, SFZ1 receives the maximum  $\angle 2$ , while SFZ1 and RAW can be adjusted to almost planar positions, corroborating that the rigidity of 2TKZ mainly comes from  $\angle 2$ .

In addition, an atomic force microscope (AFM) was used to explore the SFZn-x:Y6 blends. The surface morphology of the SFZn-x:Y6 blending film is shown in Figure S6. SFZ1-0.2:Y6 still had a high root mean square roughness ( $S_q$ ), while SFZ1-0.4:Y6 indicated a flat surface with the lowest  $S_q$ . Therefore, the flexible 3T units in polymers could effectively

reduce chain aggregation, which may prevent leading to an over-rugged morphology. SFZ2-0.2:Y6 also showed high  $S_q$ . Due to the more extended chain and low  $\Delta\epsilon$  and  $\Delta E$  of carbazole, it was easy to adjust the conformation of carbazole in a limited range, and the more extended area along the chain also facilitates molecular stretching, which would also be beneficial for the optimization of the morphology. Thus, reasonable type and the content of the second unit in polymers can regulate the morphology of the blending film.

The SFZ $n$ - $x$ :Y6 and PBDB-T-2Cl:Y6 OSC performances are explored by conventional devices (ITO/PEDOT:PSS/polymer:Y6/PDINO/Al). The current density-voltage ( $J$ - $V$ ) curves and the corresponding parameters of the devices are shown in Figure 5a and Table 2, respectively. All obtained terpolymer-based devices obtain an open-circuit voltage ( $V_{OC}$ ) > 0.84 V, a short-circuit current density ( $J_{SC}$ ) > 25 mA cm<sup>-2</sup>, and a fill factor (FF) > 63%, resulting in a PCE over 13.85%. Their FF and PCE are higher than that of PBDB-T-2Cl:Y6. Moreover, with the same designed rate ( $x = 0.2$ ) of the terpolymers, SFZ2- $x$ :Y6 devices obtain higher results ( $V_{OC}$ , FF) than SFZ1- $x$ :Y6. SFZ1-0.4:Y6 exposes highest performance ( $V_{OC} = 0.86$  V,  $J_{SC} = 26.13$  mA cm<sup>-2</sup>, FF = 69.81%, and PCE = 15.66%). Notably, the FF of OSC improved from 63.37% to 69.81%. It is well known that FF is mainly determined by the device morphology, which is significantly impacted the molecular geometries of donors and acceptors [36]. Thus, the additional flexible and rigid structure can modulate the aggregation and stacking properties of polymers [37], optimizing the morphology of the blending film and effectively enhancing the photovoltaic performance of the corresponding OSCs.

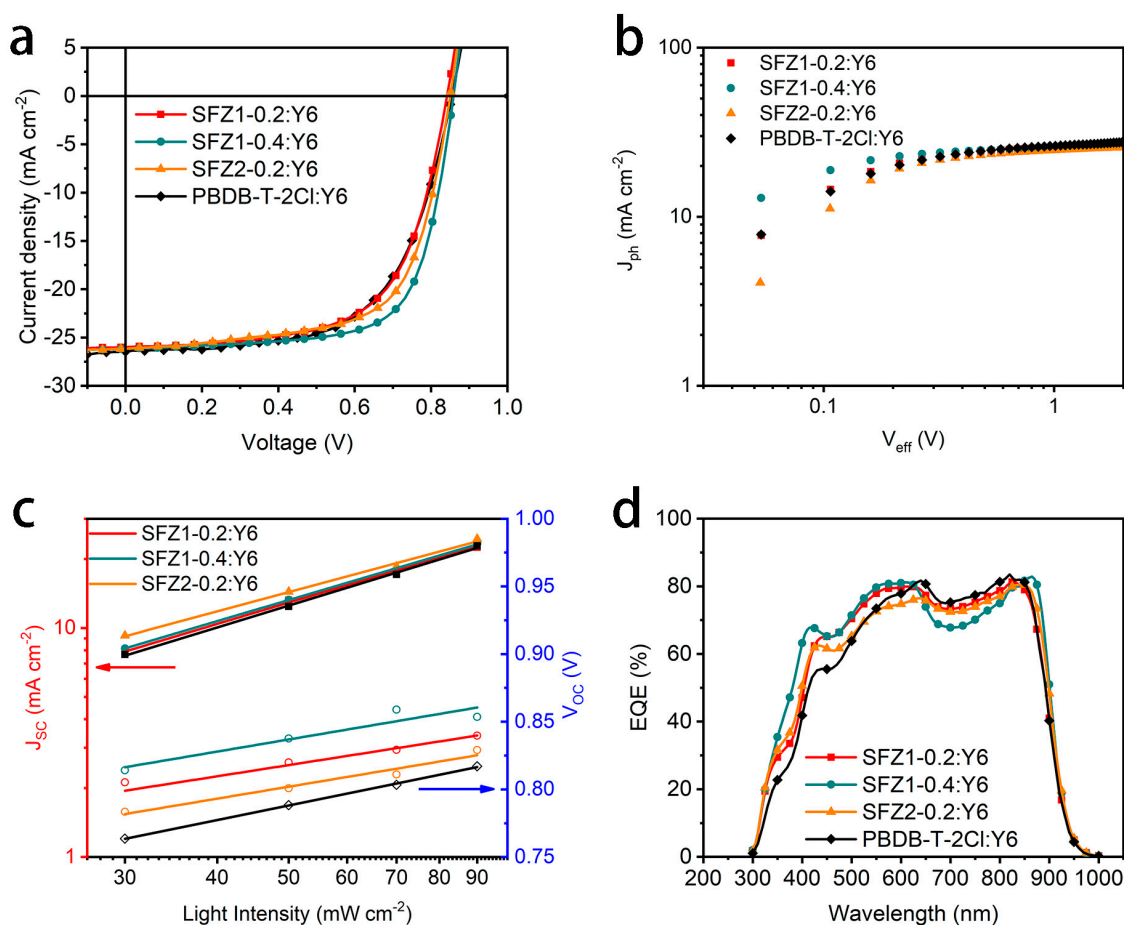


**Figure 5.** (a)  $J$ - $V$  curves, (b)  $J_{ph}$ - $V_{eff}$  curves, (c) light intensity dependence of  $J_{SC}$  and  $V_{OC}$ , (d) EQE spectra of Y6-based OSCs.

**Table 2.** Photovoltaic performance of Y6-based OSC under AM 1.5G illumination.

Polymer	V <sub>OC</sub> (V)	J <sub>SC</sub> (mA cm <sup>-2</sup> )	FF (%)	PCE <sub>max</sub> (PCE <sub>ave</sub> ) (%) <sup>a</sup>
SFZ1-0.2	0.84	25.97	63.37	13.85 (13.45)
SFZ1-0.4	0.86	26.13	69.81	15.66 (15.30)
SFZ2-0.2	0.85	26.07	65.53	14.53 (14.09)
PBDB-T-2Cl	0.83	25.96	62.76	13.54 (13.33)

<sup>a</sup> Average of 10 devices.

Moreover, the OSC processes, such as exciton dissociation, charge collection, and carrier recombination, were investigated based on SFZn-x:Y6 devices. The  $J_{ph}-V_{eff}$  relationship and the resulting exciton dissociation efficiency ( $P_{diss}$ ) and charge collection efficiency ( $P_{coll}$ ) are shown in Figure 5b and Table S3. All SFZn-x:Y6-based devices can obtain a  $P_{diss}$  close to 0.96. Thus, the additional flexible and rigid structures do not significantly decrease the exciton dissociation process in blends. In addition, SFZn-x:Y6-based devices obtained  $P_{coll}$  close to 0.8, which may be related to the fact that the introduced unfused units promote intermolecular interactions and lead to a more efficient intermolecular charge transfer process. The light intensity dependence of SFZn-x:Y6-based devices ( $J_{SC}-I$  and  $V_{OC}-I$ ) and the resulting  $\alpha$  and  $\eta$  are shown in Figure 5c and Table S3. An  $\alpha$  close to 1 corresponds to a low bimolecular recombination tendency, while low values of  $\eta$  are associated with low single-molecule or defect recombination. The SFZ1-x:Y6-based device exposes the higher  $\alpha$  and lower  $\eta$ , indicating that limited bimolecular, monomolecular, or defect recombination would have occurred during the carrier migration. The above results are similar to the higher  $J_{SC}$  of SFZ1-x:Y6-based devices.

The external quantum efficiency (EQE) spectra indicate the photoelectric conversion of the blending films for different wavelength photons (Figure 5d and Table S3). High EQE appears in the wavelength range of 350~950 nm, whose corresponding integral current density ( $J_{EQE}$ ) is about 24~25 mA cm<sup>-2</sup>. The SFZ1-0.4 device exposes the highest EQE in the 350~650 nm corresponding to the highest  $J_{EQE}$ , consistent with the highest  $J_{SC}$  obtained from the J-V curve. Therefore, all devices can achieve efficient photovoltaic conversion. In addition, the electron ( $\mu_e^-$ ) and hole ( $\mu_h^+$ ) mobilities of the SFZn-x:Y6 devices are measured by the space charge limited current (SCLC) (Figure S7 and Table S3). All  $\mu_e^-$  of the SFZn-x:Y6 devices reach the order of 10<sup>-4</sup> cm<sup>2</sup> V<sup>-1</sup> s<sup>-1</sup>, while SFZ1-x:Y6 devices indicate  $\mu_h^+$  at 10<sup>-5</sup> cm<sup>2</sup> V<sup>-1</sup> s<sup>-1</sup>. with higher  $\mu_e^-$  than  $\mu_h^+$ . Moreover, the SFZ2-0.2:Y6 device has both  $\mu_e^-$  and  $\mu_h^+$  at 10<sup>-4</sup> cm<sup>2</sup> V<sup>-1</sup> s<sup>-1</sup> resulting in a  $\mu_e^-/\mu_h^+$  approaching 1, indicating a more balanced electron and hole transport in the device, which implies the impact of additional unit selection and design on performance.

#### 4. Conclusions

In conclusion, introducing the flexible and rigid structure into the D-A polymer backbone can efficiently regulate the aggregation and stacking behavior to optimize the BHJ active layer. In polymer chains, the conformation of flexible segments can be easily adjusted by low-energy intramolecular rotation. Although the conformation of rigid chain segments is hard to convert, they may appear in a limited range of low-energy intramolecular rotations to facilitate local conformational adjustment and achieve optimization of the molecular aggregation. Such a strategy can regulate precise optimization by controlling the type and content of the introduced structure. For structures designed from thiophene and carbazole, terpolymer-based OSCs can obtain high V<sub>OC</sub> (0.84~0.86 V), J<sub>SC</sub> (25~26 mA cm<sup>-2</sup>), and FF (63~70%), resulting in PCE (13.85~15.66%).

**Supplementary Materials:** The following supporting information can be downloaded at <https://www.mdpi.com/article/10.3390/polym17020248/s1>: Figure S1: LSV curves of SFZn-x. Oxidation processes were measured from 0 V to 1.5 V and reduction processes from 0 V to −1.5 V; Figure S2: The UV-vis absorption of (a–c) SFZn-x and (d) PBDB-T-2Cl in chlorobenzene solution at different temperatures; Figure S3: Simplified structures of the polymers, whose structures are simplified to oligomers, and the alkyl group are reduced to methyl groups. (a) 2-D-A-unit D-A-D-A and the intramolecular dihedral angles of polymers ( $\angle 1$  for the dihedral angle between the BDT donor unit and  $\pi$ -bridge,  $\angle 2$  for the dihedral angle between the acceptor unit and  $\pi$ -bridge), (b) D-A and the intramolecular dihedral angles, and (c) 4-D-A-unit D-A-D-A-D-A-D-A; Figure S4: The potential energy curves of intramolecular dihedral angles of polymers in Figure S3b (a) RAW, (b) SFZ1, and SFZ2; Figure S5: The conformations of SFZ1:Y6 and SFZ2:Y6; Figure S6: Surface AFM images of SFZn-x:Y6 blending films; Figure S7:  $J^{1/2}$ -V curves by SCLC method for Y6-based devices, (a) for electron mobilities and (b) for hole mobilities. Table S1: Dihedral angles in the D and D:A conformations; Table S2: The relative energy potential ( $\Delta\epsilon$ ) and the activation energy ( $\Delta E$ ) based on potential energy curves in Figure S4; Table S3. Photovoltaic performance of the Y6-based devices.

**Author Contributions:** Methodology, X.L. (Xuebing Li), Y.Z. and A.S.; Investigation, X.J., Q.W., X.K., X.L. (Xiaojie Liu) and F.L.; Resources, F.L. and M.S.; Writing—original draft, X.J.; Writing—review & editing, M.S.; Supervision, M.S.; Funding acquisition, M.S. All authors have read and agreed to the published version of the manuscript.

**Funding:** This research work was financially supported by the National Natural Science Foundation of China (52173291), Natural Science Foundation of Shandong Province (ZR2024ME032 and ZR2024ZD15) and the Key R&D Program of Shandong Province China (2023CXGC010315).

**Institutional Review Board Statement:** Not applicable.

**Data Availability Statement:** The original contributions presented in this study are included in the article/Supplementary Materials. Further inquiries can be directed to the corresponding author.

**Conflicts of Interest:** The authors declare no conflicts of interest.

## References

1. McDowell, C.; Abdelsamie, M.; Toney, M.F.; Bazan, G.C. Solvent Additives: Key Morphology-Directing Agents for Solution-Processed Organic Solar Cells. *Adv. Mater.* **2018**, *30*, e14759. [[CrossRef](#)]
2. McAfee, S.M.; Payne, A.-J.; Hendsbee, A.D.; Xu, S.; Zou, Y.; Welch, G.C. Toward a Universally Compatible Non-Fullerene Acceptor: Multi-Gram Synthesis, Solvent Vapor Annealing Optimization, and BDT-Based Polymer Screening. *Solar RRL* **2018**, *2*, 1800143. [[CrossRef](#)]
3. Wu, Y.; Schneider, S.; Yuan, Y.; Young, R.M.; Francese, T.; Mansoor, I.F.; Dudas, P.J.; Lei, Y.; Gomez, E.D.; DeLongchamp, D.M.; et al. Twisted A-D-A Type Acceptors with Thermally-Activated Delayed Crystallization Behavior for Efficient Nonfullerene Organic Solar Cells. *Adv. Energy Mater.* **2022**, *12*, 2103957. [[CrossRef](#)]
4. Song, W.; Yu, K.; Zhou, E.; Xie, L.; Hong, L.; Ge, J.; Zhang, J.; Zhang, X.; Peng, R.; Ge, Z. Crumple Durable Ultraflexible Organic Solar Cells with an Excellent Power-per-Weight Performance. *Adv. Funct. Mater.* **2021**, *31*, 2102694. [[CrossRef](#)]
5. Chambon, S.; Derue, L.; Lahaye, M.; Pavageau, B.; Hirsch, L.; Wantz, G. MoO<sub>3</sub> Thickness, Thermal Annealing and Solvent Annealing Effects on Inverted and Direct Polymer Photovoltaic Solar Cells. *Materials* **2012**, *5*, 2521–2536. [[CrossRef](#)]
6. Du, B.; Geng, R.; Tan, W.; Mao, Y.; Li, D.; Zhang, X.; Liu, D.; Tang, W.; Huang, W.; Wang, T. Heating induced aggregation in non-fullerene organic solar cells towards high performance. *J. Energy Chem.* **2021**, *54*, 131–137. [[CrossRef](#)]
7. Alam, S.; Aldosari, H.; Petoukhoff, C.E.; Vary, T.; Althobaiti, W.; Alqurashi, M.; Tang, H.; Khan, J.I.; Nadazdy, V.; Mueller-Buschbaum, P.; et al. Thermally-Induced Degradation in PM6:Y6-Based Bulk Heterojunction Organic Solar Cells. *Adv. Funct. Mater.* **2024**, *34*, 2308076. [[CrossRef](#)]
8. Huettner, S.; Sommer, M.; Chiche, A.; Krausch, G.; Steiner, U.; Thelakkat, M. Controlled solvent vapour annealing for polymer electronics. *Soft Matter* **2009**, *5*, 4206–4211. [[CrossRef](#)]
9. Liu, J.; Zhou, W.; Deng, J.; Geng, X.; Jeong, S.Y.; Cui, Y.; Woo, H.Y.; Wu, F.; Liu, F.; Chen, L. Dimerized small molecular acceptors: Regulation of dimer conformation realizes binary organic solar cells with highly comprehensive performance. *Nano Energy* **2024**, *121*, 109218. [[CrossRef](#)]

10. Zhang, Z.-G.; Wang, J. Structures and properties of conjugated Donor-Acceptor copolymers for solar cell applications. *J. Mater. Chem.* **2012**, *22*, 4178–4187. [CrossRef]
11. Hu, W.B. *Polymer Physics: A Molecular Approach*; Springer: Vienna, Austria, 2013. [CrossRef]
12. Peng, Z.; Ye, L.; Ade, H. Understanding, quantifying, and controlling the molecular ordering of semiconducting polymers: From novices to experts and amorphous to perfect crystals. *Mater. Horiz.* **2022**, *9*, 577–606. [CrossRef]
13. Wang, Q.; Wang, Y.; Zheng, W.; Shahid, B.; Qiu, M.; Wang, D.; Zhu, D.; Yang, R. Regulating Molecular Aggregations of Polymers via Ternary Copolymerization Strategy for Efficient Solar Cells. *ACS Appl. Mater. Interfaces* **2017**, *9*, 32126–32134. [CrossRef]
14. Zheng, Z.; Yao, H.; Ye, L.; Xu, Y.; Zhang, S.; Hou, J. PBDB-T and its derivatives: A family of polymer donors enables over 17% efficiency in organic photovoltaics. *Mater. Today* **2020**, *35*, 115–130. [CrossRef]
15. Das, S.; Senanayak, S.P.; Bedi, A.; Narayan, K.S.; Zade, S.S. Synthesis and charge carrier mobility of a solution-processable conjugated copolymer based on cyclopenta[c]thiophene. *Polymer* **2011**, *52*, 5780–5787. [CrossRef]
16. Avila, H.C.; Serrano, P.; Barreto, A.R.J.; Ahmed, Z.; Gouvêa, C.P.; Vilani, C.; Capaz, R.B.; Marchiori, C.F.N.; Cremona, M. High hole-mobility of rrP3HT in organic field-effect transistors using low polarity polyurethane gate dielectric. *Org. Electron.* **2018**, *58*, 33–37. [CrossRef]
17. Bi, P.; Ren, J.; Zhang, S.; Wang, J.; Hou, J. PTV-based p-type organic semiconductors: Candidates for low-cost photovoltaic donors with simple synthetic routes. *Polymer* **2020**, *209*, 122900. [CrossRef]
18. Huang, S.; Huang, X.; Chen, L.; Liao, Z.; Ding, S.; Yuan, Z.; Chen, Y. A rational comparison of the effects of halogen atoms incorporated into the polymer donors on the performance of polymer solar cells. *Org. Electron.* **2019**, *70*, 86–92. [CrossRef]
19. He, Z.; Li, S.; Zeng, R.; Lin, Y.; Zhang, Y.; Hao, Z.; Zhang, S.; Liu, F.; Tang, Z.; Zhong, H. Binary Organic Solar Cells with Exceeding 19% Efficiency via the Synergy of Polyfluoride Polymer and Fluorous Solvent. *Adv. Mater.* **2024**, *36*, 2404824. [CrossRef]
20. Ran, G.; Su, W.; Lu, H.; Liu, Y.; Bo, Z.; Zhang, W. Intrachain and Interchain Excited-State Dynamics of Temperature-Dependent Aggregation Copolymer in Solution. *J. Phys. Chem. B* **2022**, *126*, 7393–7399. [CrossRef]
21. Valeev, E.F. Libint: A Library for the Evaluation of Molecular Integrals of Many-Body Operators over Gaussian Functions. Version 2.4.1. Available online: <http://libint.valeev.net/> (accessed on 1 January 2025).
22. Lehtola, S.; Steigemann, C.; Oliveira, M.J.T.; Marques, M.A.L. Recent developments in LIBXC—A comprehensive library of functionals for density functional theory. *SoftwareX* **2018**, *7*, 1–5. [CrossRef]
23. Kruse, H.; Grimme, S. A geometrical correction for the inter- and intra-molecular basis set superposition error in Hartree-Fock and density functional theory calculations for large systems. *J. Chem. Phys.* **2012**, *136*, 154101. [CrossRef]
24. Caldeweyher, E.; Bannwarth, C.; Grimme, S. Extension of the D3 dispersion coefficient model. *J. Chem. Phys.* **2017**, *147*, 034112. [CrossRef]
25. Caldeweyher, E.; Ehlert, S.; Hansen, A.; Neugebauer, H.; Spicher, S.; Bannwarth, C.; Grimme, S. A generally applicable atomic-charge dependent London dispersion correction. *J. Chem. Phys.* **2019**, *150*, 154122. [CrossRef]
26. Grimme, S.; Hansen, A.; Ehlert, S.; Mewes, J.-M. r(2)SCAN-3c: A “Swiss army knife” composite electronic-structure method. *J. Chem. Phys.* **2021**, *154*, 064103. [CrossRef]
27. Furness, J.W.; Kaplan, A.D.; Ning, J.; Perdew, J.P.; Sun, J. Accurate and Numerically Efficient r(2)SCAN Meta-Generalized Gradient Approximation. *J. Phys. Chem. Lett.* **2020**, *11*, 8208–8215; Erratum in *J. Phys. Chem. Lett.* **2020**, *11*, 9248. [CrossRef]
28. Zhang, S.; Qin, Y.; Zhu, J.; Hou, J. Over 14% Efficiency in Polymer Solar Cells Enabled by a Chlorinated Polymer Donor. *Adv. Mater.* **2018**, *30*, e1800868. [CrossRef]
29. Inoue, K.; Ishiwari, F.; Fukushima, T. Selective synthesis of diazacyclooctane-containing flexible ladder polymers with symmetrically or unsymmetrically substituted side chains. *Polym. Chem.* **2020**, *11*, 3690–3694. [CrossRef]
30. Plimpton, S. Fast Parallel Algorithms for Short-Range Molecular Dynamics. *J. Comput. Phys.* **1995**, *117*, 1–19. [CrossRef]
31. Thompson, A.P.; Aktulga, H.M.; Berger, R.; Bolintineanu, D.S.; Brown, W.M.; Crozier, P.S.; In’t Veld, P.J.; Kohlmeyer, A.; Moore, S.G.; Nguyen, T.D.; et al. LAMMPS—a flexible simulation tool for particle-based materials modeling at the atomic, meso, and continuum scales. *Comput. Phys. Commun.* **2022**, *271*, 108171. [CrossRef]
32. Wang, C.; Li, W.; Liao, K.; Wang, Z.; Wang, Y.; Gong, K. AuToFF Program, Vesion 1.0. Hzwtech. Shanghai 2023. Available online: <https://cloud.hzwtech.com/web/product-service?id=36> (accessed on 1 January 2025).
33. Martinez, L.; Andrade, R.; Birgin, E.G.; Martinez, J.M. PACKMOL: A Package for Building Initial Configurations for Molecular Dynamics Simulations. *J. Comput. Chem.* **2009**, *30*, 2157–2164. [CrossRef]
34. Kaminski, G.A.; Friesner, R.A.; Tirado-Rives, J.; Jorgensen, W.L. Evaluation and reparametrization of the OPLS-AA force field for proteins via comparison with accurate quantum chemical calculations on peptides. *J. Phys. Chem. B* **2001**, *105*, 6474–6487. [CrossRef]
35. Jorgensen, W.L.; Maxwell, D.S.; TiradoRives, J. Development and testing of the OPLS all-atom force field on conformational energetics and properties of organic liquids. *J. Am. Chem. Soc.* **1996**, *118*, 11225–11236. [CrossRef]

36. Wang, Y.; Zhong, H.; Hong, Y.; Shan, T.; Ding, K.; Zhu, L.; Liu, F.; Wei, H.; Yu, C.; Zhong, H. Tailoring the molecular geometry of polyfluoride perylene diimide acceptors towards efficient organic solar cells. *J. Mater. Chem. C* **2020**, *8*, 8224–8233. [[CrossRef](#)]
37. Rubio Arias, J.J.; MotanAff, I.C.; Albuquerque, L.S.; Dahmouche, K.; Vieira Marques, M.d.F. A GIWAXS study of crystallization in annealed conjugated polymers presenting technological interest for organic solar cell applications. *J. Mater. Sci.-Mater. Electron.* **2022**, *33*, 1838–1850. [[CrossRef](#)]

**Disclaimer/Publisher’s Note:** The statements, opinions and data contained in all publications are solely those of the individual author(s) and contributor(s) and not of MDPI and/or the editor(s). MDPI and/or the editor(s) disclaim responsibility for any injury to people or property resulting from any ideas, methods, instructions or products referred to in the content.